JOURNAL OF AIRCRAFT
Vol. 35, No. 1, January–February 1998

Pitch Rate and Reynolds Number Effects on Unsteady Boundary-Layer Transition and Separation

Scott J. Schreck*
U.S. Air Force Office of Scientific Research, Bolling Air Force Base, Washington, D.C. 20332
William E. Faller†
Johns Hopkins University, Baltimore, Maryland 21218
and
Hank E. Helin‡
U.S. Air Force Operational Test and Evaluation Center, Kirtland Air Force Base, New Mexico 87117

A NACA 0015 airfoil was pitched at a constant rate through static stall to elevated angles of attack. Shear stress measurements of high spatial and temporal resolution were performed near the airfoil leading edge, in the vicinity of subsequent dynamic stall vortex initiation. Using these data, unsteady boundary-layer reversal and transition were characterized for a range of nondimensional pitch rates and Reynolds numbers. Analyses revealed the independent influences of nondimensional pitch rate and Reynolds number upon unsteady boundary-layer reversal and transition. Temporal and spatial relationships between unsteady boundary-layer reversal and transition imply that unsteady boundary-layer reversal is a precursor and principal determinant in unsteady boundary-layer transition. Comprehension of these and other fundamental unsteady flow physics are crucial for the control of dynamically separated flows generated by maneuvering aircraft, rotorcraft, and wind energy machines.

Nomenclature

c = airfoil chord length, cm
Re_c = chord Reynolds number
s = distance from leading edge along airfoil surface, cm
t = time, s
t_{nd} = nondimensional time, tU_∞/c
U_∞ = test section velocity, m/s
x = distance from leading edge along airfoil chord, cm
α = instantaneous angle of attack, deg
α^+ = nondimensional pitch rate, $c(d\alpha/dt)/U_\infty$
$d\alpha/dt$ = pitch rate, rad/s

Introduction

POTENTIAL performance enhancements to maneuvering aircraft, rotorcraft, and wind energy machines continue to prompt intense study of dynamically separated flowfields. When a lifting surface pitches through static stall to elevated angles of attack, the unsteady boundary layer dynamically separates near the leading edge and gives rise to an energetic unsteady vortex. This vortex grows as it convects downstream over the lifting surface and is finally shed into the wake. Associated with vortex initiation, growth, and shedding is brief but substantial lift augmentation followed by catastrophic stall. If thoroughly understood and properly controlled, dynamically separated flows have the potential to confer dramatic performance enhancements upon systems impacted by dynamic separation.

Presented as Paper 94-2256 at the AIAA 25th Fluid Dynamics, Plasmadynamics, and Laser Conference, Colorado Springs, CO, June 20–23, 1994; received Aug. 28, 1996; revision received July 9, 1997; accepted for publication July 23, 1997.

*Program Manager, 110 Duncan Avenue, Room B115. Member AIAA.
†Research Faculty, Department of Mechanical Engineering. Member AIAA.
‡Program Manager, 8500 Gibson Boulevard SE. Member AIAA.

Much effort has been directed toward characterizing and understanding dynamically separated flows.[1] In spite of this, limited success has been attained in controlling unsteady flowfields dominated by large, energetic vortices. However, preventing or delaying leading-edge vortex initiation would facilitate control of dynamically separated flows by extending lift enhancement. Thus, clarified understanding of unsteady boundary-layer separation would accelerate progress toward dynamically separated flow control.[2]

Previous investigations have identified significant aspects of unsteady boundary-layer separation, especially unsteady boundary-layer reversal. Carr et al.[3] experimentally isolated three distinct types of unsteady boundary-layer reversal on an oscillating airfoil, all of which led to classical dynamic stall. In another experiment, Schreck and Luttges[4] observed that reverse flows originating near the trailing edge of a pitching airfoil were incidental to unsteady boundary-layer reversal and vortex initiation near the leading edge.

Calculations by Visbal[5] showed that a thin boundary-layer reversal region played a crucial role in leading-edge vortex initiation on a pitching airfoil. Interaction between this reverse flow layer and the downstream flowing layer above it elicited a strong shear layer, which culminated in leading-edge vortex inception. Numerical work by Ghia et al.[6] linked size and strength of the unsteady boundary-layer reversal to strength and formation time of the leading-edge vortex. Knight and Choudhuri[7] computed the topology of two-dimensional unsteady boundary-layer reversal for a pitching airfoil. They correlated the appearance of critical points in the topology to reverse flow regions and leading-edge vortex emergence.

The prominent influence of transition on unsteady flowfields has been affirmed by Ericsson[8] for both attached and separated unsteady flows. Lorber and Carta[9] experimentally characterized unsteady boundary-layer transition and relaminarization on a pitching wing. Wilder et al.[10] experimentally demonstrated that the dynamic stall process is quite sensitive to the boundary-layer turbulence state. Carr and Cebeci[11] showed numerically that dynamic stall significantly changes transition location on a pitching airfoil.

The current experiment employs time-dependent shear stress measurements to characterize unsteady boundary-layer reversal and transition in the vortex initiation region on a pitching airfoil. Alterations to experimental parameters prompted orderly variations in unsteady boundary-layer reversal and transition. Using this information, physical mechanisms responsible for these events were postulated.

Experimental Methods

Unsteady shear stress measurements were performed in the Frank J. Seiler 0.91 m × 0.91 m low-speed wind tunnel located at the U.S. Air Force Academy. Figure 1 shows a planform view of the model configuration used in these experiments. The NACA 0015 airfoil was fabricated from hollow aluminum airfoil stock, having a chord length of 15.24 cm and a span length of 76.84 cm. Each end of the airfoil was fitted with a circular splitter plate that was 0.32 cm thick, 30.48 cm in diameter, and machined to a sharp edge around the perimeter.

The model was mounted vertically in the center of the test section. Both the upper and lower ends of the model were connected to steel shafts mounted in ball bearings. Airfoil pitching was driven through the lower shaft, which was connected to a 3.5-hp stepper motor through a 4:1 gear linkage. Airfoil pitch axis was located at 0.25c throughout these experiments.

This investigation employed U_∞ = 6.10, 12.19, and 24.38 m/s, corresponding to $Re_c = 4.6 \times 10^4$, 9.2×10^4, and 1.84×10^5. The airfoil was pitched at rates of 183, 367, and 733 deg/s, yielding $\alpha^+ = 0.04$, 0.08, and 0.16, respectively. For each parameter combination, 20 consecutive airfoil pitch motions were sampled and ensemble averaged. Static α measurements were also performed at all three Re_c.

A thin-film, multiple-element, conformal array of shear stress sensors was applied to the airfoil surface using an aerosol adhesive. Array orientation placed the sensor row parallel to the chord line and 40.64 cm below the upper end of the airfoil, as shown in Fig. 1. The array wrapped around the entire airfoil contour, and the array edges were located at the airfoil trailing edge. This prevented the array from introducing irregularities on the airfoil surface. Individual nickel sensor elements on the array were 1.65 mm long (spanwise direction), 0.13 mm wide (chordwise direction), and 0.3 μm thick. Nominal sensor cold resistance was 6.0 Ω. The entire array contained a total of 15 sensors spaced 2.54 mm apart (chordwise direction). Figure 2 shows the locations of these sensors on the airfoil section. This diagram depicts the leading 0.25c of the airfoil, with the sensor farthest forward located at the airfoil leading edge. Construction and use of these thin-film arrays are described in detail by Stack et al.[12] and Mangalam et al.[13]

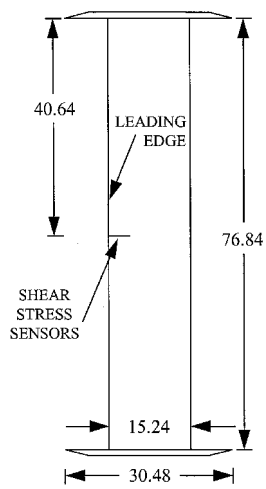

Fig. 1 Planform view of airfoil model. All dimensions are stated in centimeters.

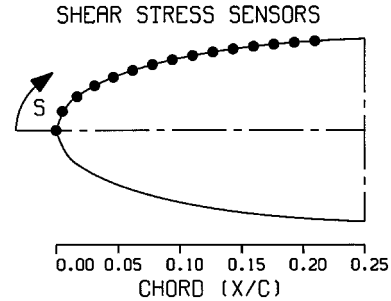

Fig. 2 Cross section of NACA 0015 airfoil leading-edge region showing shear stress sensor locations.

Each of the 15 sensors was connected to a separate constant temperature thermal anemometer circuit. Anemometer overheat resistance ratios were set at 1.10. Separate experiments determined that sensor element heat fluxes at this overheat ratio were low enough to avoid tripping either the steady or unsteady boundary layers examined in the current investigation. Anemometer bandwidths were set at 10 kHz using the square wave test.

To increase the dynamic range of acquired data, the anemometer signals were routed through bias subtraction modules prior to amplification and data acquisition. The bias subtraction circuit was designed to maximize signal-to-noise ratio and reliability by minimizing the number of active circuit components. These requirements were successfully achieved at the minor expense of inverted output signal. Validation tests confirmed a flat frequency response beyond 10 kHz. After bias cancellation, signals were low-pass filtered (1 kHz cutoff) and amplified by a gain between 20 and 100. Gain selection was dictated by signal magnitudes and an A/D converter input range. The resulting signals were then sampled and digitized at 2 kHz by a data acquisition system having a 12-bit A/D converter.

Prior to acquiring the data presented herein, systematic validation tests were carried out. Initial tests at a fixed airfoil angle of attack and constant test section velocity demonstrated that the system described in the preceding text remained stable during extended periods of operation. Further, ambient temperature was well controlled and fluctuations were negligible. Calibrations to establish a quantitative relationship between surface shear stress and output signal level were not attempted. However, straightforward procedures unambiguously established the qualitative correspondence between shear stress variation and recorded signal level excursion. With the airfoil held at zero angle of attack, the output signal was recorded during slow variations in test section velocity. This confirmed that, for the system configured as described earlier, decreasing shear stress prompted increasing signal levels, and vice versa.

Results and Discussion

Airfoil Pitching Motions

Throughout the current investigation, all dynamic experiments employed constant rate airfoil pitching motions that began at α = 0.0 deg and ended at α = 60.0 deg. The start of airfoil pitching coincided with the inception of shear stress data acquisition. None of the pitching motions suffered from prominent nonlinearity, or from appreciable acceleration or deceleration transients.[14,15] Constant rate airfoil pitching elicited pronounced fluctuations in unsteady shear stress. Specific features in the data were associated with unsteady boundary-layer reversal and transition.

Steady Boundary-Layer Data and Analysis

To characterize steady boundary-layer development, the airfoil was incremented through 25 static angles of attack. Figure 3 shows a representative graph of anemometer output signal vs static α for all 15 shear stress sensors. U_∞ was 12.19 m/s,

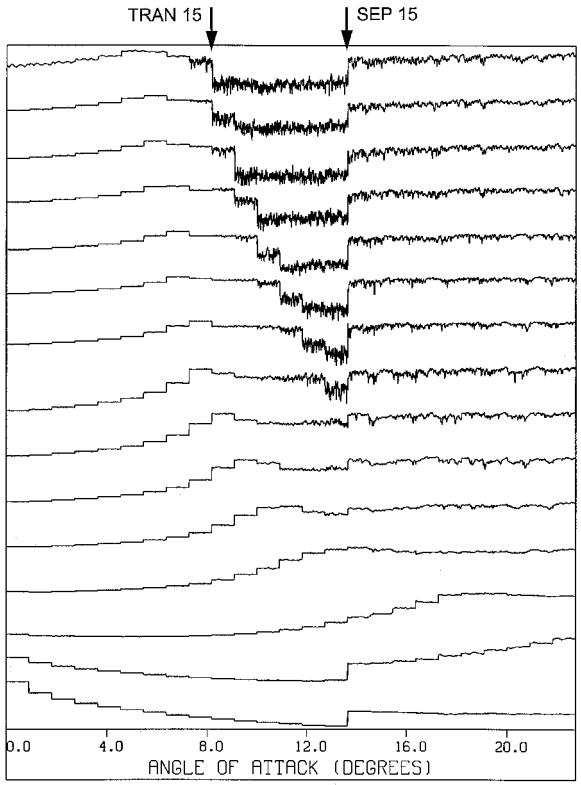

Fig. 3 Static α shear stress histories for $Re_c = 9.2 \times 10^4$. Occurrence of transition and separation at sensor 15 are indicated by TRAN 15 and SEP 15.

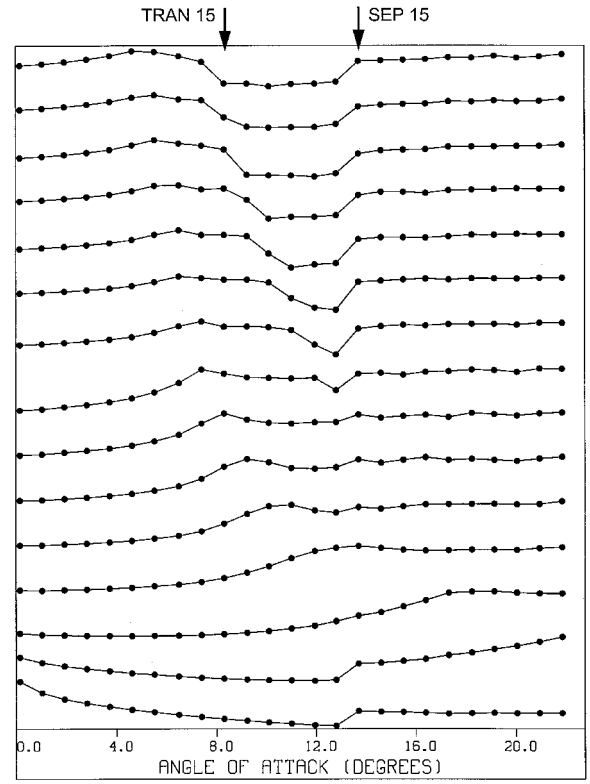

Fig. 4 Ensemble-averaged static α shear stress vs α for $Re_c = 9.2 \times 10^4$. Occurrence of transition and separation at sensor 15 are indicated by TRAN 15 and SEP 15.

yielding $Re_c = 9.2 \times 10^4$. The bottom trace corresponds to the shear stress sensor at the airfoil leading edge, and the 14 successively higher traces represent the 14 sensors farther aft on the airfoil. Each of the 15 traces is composed of 25 subintervals. Each subinterval, corresponding to one static α, contains 100 data samples acquired at 2 kHz. For each subinterval, α corresponds to the value on the horizontal axis at the left end of the subinterval. Low signal levels indicate elevated shear stress, whereas high signal levels correspond to reduced shear stress. Signal magnitude has been normalized for all traces and absolute references have been omitted.

In Fig. 3, plots 1 and 2 initially decrease gradually in response to higher α. This trend is abruptly halted at α = 13.6 deg, when signal levels increase substantially on plots 1 and 2, indicating a pronounced decrease in shear stress levels. The marked decline in shear stress on plots 1 and 2 is closely correlated with similar behaviors in traces 8–15, discussed next. Thereafter, plot 1 remains level with higher α, indicating constant shear stress levels, while plot 2 rises gradually, signaling a moderate decrease in shear stress.

Also in Fig. 3, plots 3–15 exhibit behaviors that are significantly different from plots 1 and 2. Increasing α initially prompts gradually rising signal levels on channels 3–15. This indicates reduced heat transfer caused by decreasing surface shear stress that is prompted by boundary-layer thickening. Subsequently, signal levels reach maxima, corresponding to shear stress minima. Following attainment of these shear stress minima, the subintervals on traces 8–15, between α = 8.2 and 13.6 deg, show sharply decreasing mean levels accompanied by substantially greater signal variability. These signal attributes represent higher mean shear stress and greater shear stress variation, indicating boundary-layer transition. This event occurred later for locations farther forward on the airfoil, indicating that transition moved steadily forward with increasing α. Finally, at sensors 8–15, signal levels increase substantially, indicating prominent decreases in mean shear stress while shear stress variability undergoes moderate attenuation. This event occurs at α = 13.6 deg for sensors 8–15 and corresponds to steady boundary-layer separation.

The shear stress data in Fig. 3 were ensemble averaged and are shown in Fig. 4. The 100 data samples in each of the 25 subintervals have been ensemble averaged, yielding 25 discrete points for each of the 15 traces. Ensemble averaging clarifies the forward movement of boundary-layer transition with increasing α, as indicated by the pronounced decrease in traces 8–15, between α = 8.2 and 13.6 deg. Ensemble averaging also shows steady boundary-layer separation as the prominent rise in traces 8–15 at α = 13.6 deg.

Unsteady Boundary-Layer Data and Analysis

Figure 5 contains raw data for $\alpha^+ = 0.08$ and $Re_c = 9.2 \times 10^4$. Plot no. 1 shows airfoil α increase with time, whereas plot nos. 2–16 record unsteady shear stress histories at shear stress sensors 1–15. All 16 plots consist of 20 superimposed traces corresponding to 20 consecutive airfoil pitching motions. The left end of the horizontal axis corresponds to the inception of airfoil pitching and time increases to the right. Vertical axis scaling is arbitrary. As in Figs. 3 and 4, higher anemometer output signals in Fig. 5 correspond to lower shear stress.

In Fig. 5, unsteady shear stress initially increased progressively on plot nos. 2 and 3 (sensors 1 and 2), reached maxima, and then decreased again. On plot nos. 5–16 (sensors 4–15), unsteady shear stress first decreased as the airfoil pitched up. The shear stresses quickly reached minima, as indicated by the maxima in anemometer output signal, and began to increase. As shear stresses increased, the signals became more irregular, indicating greater variability in unsteady shear stress between successive airfoil pitch motions.

Ensemble averaging of raw unsteady shear stress data similar to those presented in Fig. 5 yielded graphs similar to Fig. 6. In Fig. 6, $\alpha^+ = 0.08$ and $Re_c = 9.2 \times 10^4$. Signals from sensor 1 appear in the bottom trace, and signals from sensors progressively farther aft on the airfoil are shown in successively higher traces. The inception of airfoil pitching corre-

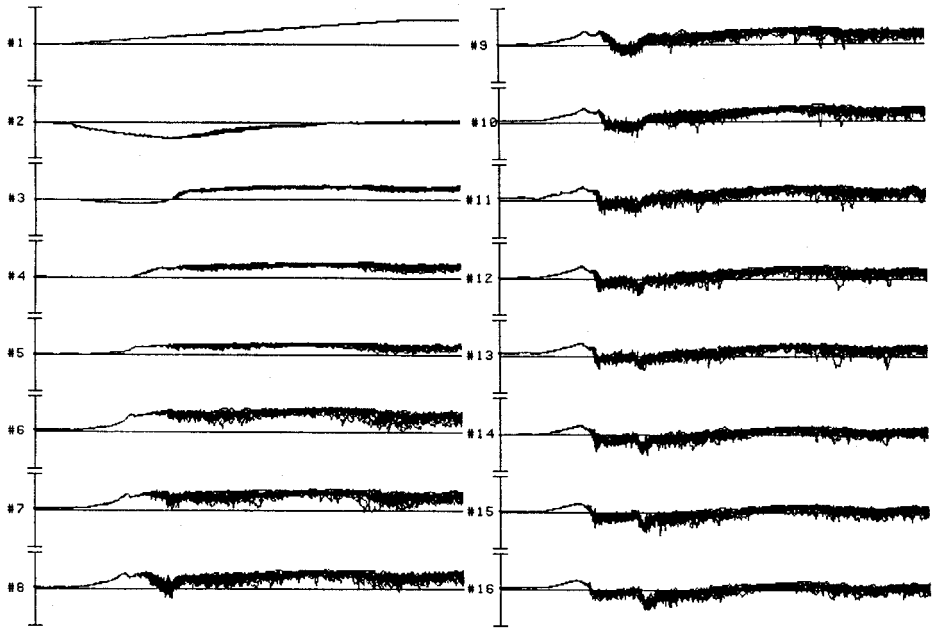

Fig. 5 Unsteady shear stress histories for $\alpha^+ = 0.08$ and $Re_c = 9.2 \times 10^4$. Pitch angle history is recorded on trace no. 1. Shear stress histories are recorded in trace nos. 2–16.

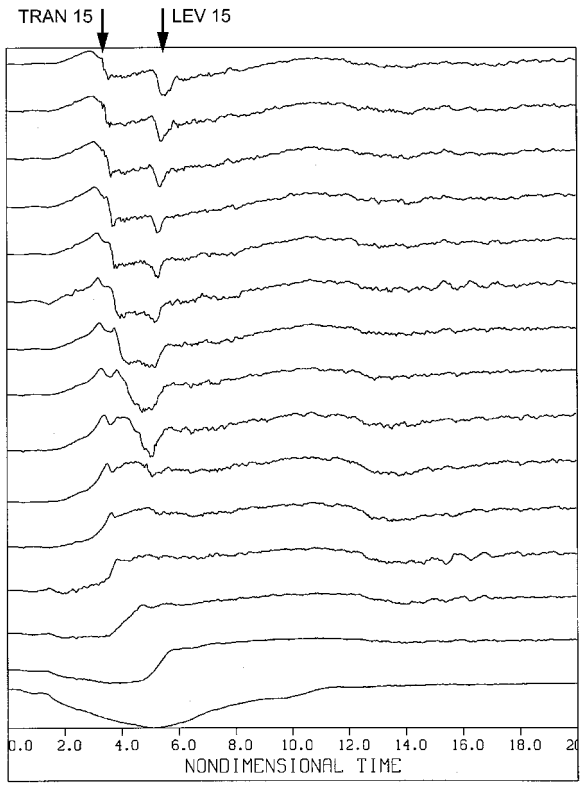

Fig. 6 Ensemble-averaged unsteady shear stress histories for $\alpha^+ = 0.08$ and $Re_c = 9.2 \times 10^4$. Occurrence of transition and leading-edge vortex passage at sensor 15 are indicated by TRAN 15 and LEV 15.

sponds to $t_{nd} = 0.0$. Scale on the vertical axis is arbitrary because signal magnitude has been normalized for all traces and absolute references have been omitted. As in previous shear stress graphs, higher output signal levels indicate lower shear stress. In addition to shear stress ensemble-average histories, shear stress standard deviation histories were also computed from the raw data like those presented in Fig. 5, but are not shown herein.

In Fig. 6, as airfoil pitching began, unsteady shear stress initially increased gradually on plots 1 and 2 and attained maxima before decreasing again. At sensors 3–15, unsteady boundary-layer thickening prompted shear stress to first progressively decrease with higher α. These decreases culminated in shear stress minima at these same sensor locations, which occurred between $t_{nd} = 2.93$ and 3.84. Subsequently, plots 7–15 show a gradual decrease corresponding to a gradual unsteady shear stress rise over the same airfoil region, beginning at the sensor farthest aft. Shortly thereafter, the gradual declines in plots 7–15 were supplanted by significantly sharper descents, indicating sudden shear stress increases. These sudden shear stress increases were closely correlated with sudden, brief increases in signal standard deviation, and correspond to unsteady boundary-layer transition. Accelerated shear stress rise was suddenly interrupted and followed by a period during which unsteady shear stress remained approximately constant. This period was terminated by well-defined signal level minima that occurred at sensors 6–15 between $t_{nd} = 5.03$ and 5.63. These minima, corresponding to shear stress maxima, were caused by the passage of the nascent leading-edge vortex.

Unsteady Boundary-Layer Reversal

Unsteady boundary-layer reversal produced no prominent shear stress extrema or variations in signal level. However, a technique developed by Stack et al.[12] and Mangalam et al.[13] for locating steady boundary-layer separation, was extended to the unsteady regime to detect unsteady boundary-layer reversal. In this technique, shear stress records from two adjacent sensors are examined for phase reversals. When a flow structure or event is located on the same side of two sensors, movement of this structure or event along the surface will exercise the same influence on both sensors. As such, time variations in the shear stress records corresponding to these two sensors will be in phase. Alternatively, when a flow structure or event is situated between two sensors, motion along the surface will have opposing influences on these two sensors. Thus, time variations in the shear stress records for these two sensors will be out of phase. When two signals exhibit a 180-deg phase relationship, this indicates that boundary-layer reversal has occurred between the two corresponding sensors.[12,13]

Figure 7 shows representative unsteady shear stress fluctuations at two adjacent shear stress sensors. Pairs of vertical lines connected by solid bars indicate representative phase reversal episodes between the two shear stress histories. For each combination of Re_c and α^+, data similar to those plotted in Fig.

6 were searched visually for phase reversals. For each parameter combination, the α at which phase reversal initially occurred was plotted for each sensor pair. The results are contained in Figs. 8 and 9.

In Fig. 8, initial unsteady boundary-layer reversal is plotted against α over the experimental range of α^+, for $Re_c = 9.2 \times 10^4$. For $\alpha^+ = 0.04$, unsteady boundary-layer reversal was first detected at $0.184s/c$ at $\alpha = 9.97$ deg, and moved forward at a constant rate to $0.134s/c$ as α increased. There, reversal continued forward in response to increasing α, decelerating to a lower constant rate and terminating at $0.067s/c$. At $\alpha^+ = 0.08$, unsteady boundary-layer reversal was first observed at $0.200s/c$ at $\alpha = 11.71$ deg and proceeded forward in an erratic fashion with increasing α to $0.134s/c$. There, the forward progress of boundary-layer reversal slowed and continued forward at an approximately constant speed to $0.067s/c$. At $\alpha^+ = 0.16$, a different progression of unsteady boundary-layer reversal was seen. Reversal was first observed simultaneously at 0.167 and $0.184s/c$, at $\alpha = 15.03$ deg. From there, reversal moved both forward and aft on the airfoil with increasing α.

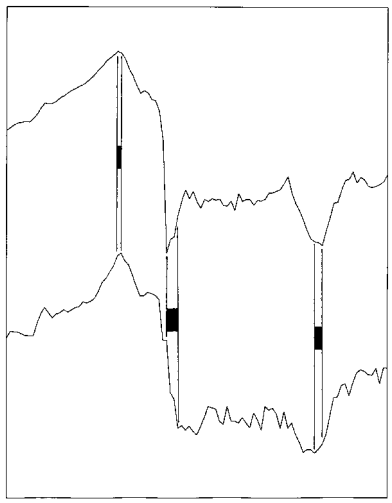

Fig. 7 Representative phase reversal episodes for two adjacent shear stress sensors. Pairs of vertical lines connected by thick horizontal bars demarcate 180-deg phase relationship between the two shear stress histories.

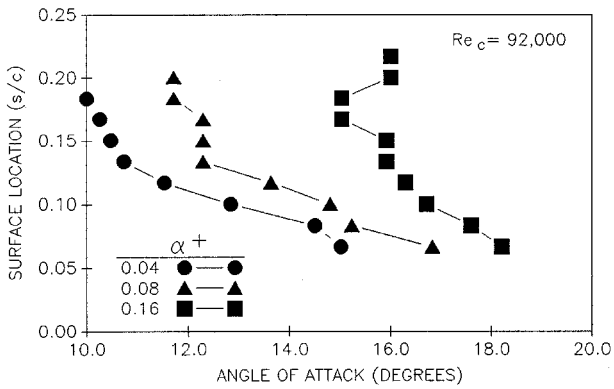

Fig. 8 Summary plot of unsteady boundary-layer reversal location vs α for $Re_c = 9.2 \times 10^4$ and experimental range of α^+.

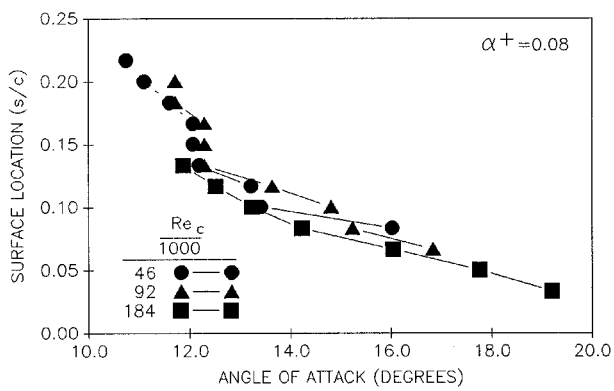

Fig. 9 Summary plot of unsteady boundary-layer reversal location vs α for $\alpha^+ = 0.08$ and experimental range of Re_c.

Greater leading-edge localization of unsteady boundary-layer reversal with increasing α^+ is consistent with the more strongly focused pressure gradients seen in computational[16] and experimental[4,17] results and conforms with existing vorticity models.[18] Higher α^+ also delayed unsteady boundary-layer reversal to higher α, consistent with delays imposed by boundary-layer viscosity.[14] Finally, plot slopes in Fig. 8 are consistently steeper for higher α^+. This indicates that boundary-layer reversal progression at higher α^+ is more responsive to α increases and moves at a higher speed.

Figure 9 plots initial unsteady boundary-layer reversal against α over the experimental range of Re_c, for $\alpha^+ = 0.08$. For $Re_c = 4.6 \times 10^4$, unsteady boundary-layer reversal was initially observed at $0.217s/c$ at $\alpha = 10.74$ deg, and moved forward with increasing α, reaching $0.083s/c$ at $\alpha = 16.02$ deg. At $Re_c = 9.2 \times 10^4$, unsteady boundary-layer reversal first appeared at a surface location of $0.200s/c$, and moved forward to $0.067s/c$ as α increased from 11.71 to 16.83 deg. At $Re_c = 4.6 \times 10^4$ and 9.2×10^4, forward progress of boundary-layer reversal briefly underwent dramatic acceleration while passing between 0.167 and $0.134s/c$. For $Re_c = 1.84 \times 10^5$, unsteady boundary-layer reversal was initially detected at $0.134s/c$ at $\alpha = 11.87$ deg, and ended at $0.033s/c$ at $\alpha = 19.20$ deg. At $Re_c = 1.84 \times 10^5$, unsteady boundary-layer reversal moved steadily forward at approximately constant velocity with no prominent disruption.

Increasing Re_c delayed the initial occurrence of unsteady boundary-layer reversal to higher α. In addition, greater Re_c also moved the initial unsteady boundary-layer reversal closer to the airfoil leading edge and compressed the surface length over which unsteady boundary-layer reversal moved after the initial occurrence. Forward movement and compression of the unsteady boundary-layer reversal region with increasing Re_c is consistent with the stronger, more focused leading-edge pressure gradients that develop prior to the leading-edge vortex inception at higher Re_c.[17,18]

Unsteady Boundary-Layer Transition

Unsteady boundary-layer transition was indicated by a rapid increase in mean shear stress accompanied by a brief but pronounced maximum in shear stress standard deviation.[9] For each combination of Re_c and α^+, the α at which unsteady boundary-layer transition occurred was plotted for each sensor. The results are contained in Figs. 10 and 11.

In Fig. 10, unsteady boundary-layer transition location is plotted vs α over the experimental range of α^+, for $Re_c = 9.2$

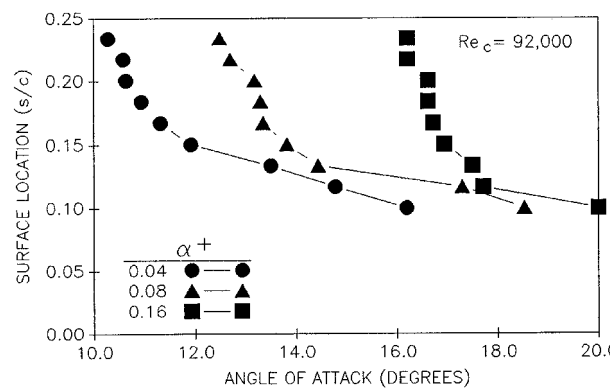

Fig. 10 Summary plot of unsteady boundary-layer transition location vs α for $Re_c = 9.2 \times 10^4$ and experimental range of α^+.

$\times 10^4$. For all three α^+, transition was first observed at the sensor farthest aft, at $0.234s/c$, and progressed forward with increasing α to $0.100s/c$. Unsteady boundary-layer transition was consistently delayed to higher α for greater α^+. Unsteady boundary-layer transition first occurred at α = 10.28, 12.48, and 16.20 deg for α^+ = 0.04, 0.08, and 0.16, respectively.

In Fig. 10, the general pattern of transition movement in response to the α increase was similar for all three α^+. In all three cases, unsteady boundary-layer transition initially moved forward at an approximately constant rate. When the transition point reached some intermediate surface location, forward movement decelerated significantly and then continued forward at a slower constant speed. The surface location where this deceleration occurred moved forward with increasing α^+, and occurred at 0.167, 0.134, and $0.117s/c$ for α^+ = 0.04, 0.08, and 0.16, respectively. Finally, prior to deceleration, plot slopes in Fig. 10 are only slightly steeper at higher α^+. This indicates that unsteady boundary-layer transition movement is only slightly more responsive to α increments at higher α^+. However, transition progression speed increases substantially with higher α^+.

Figure 11 plots unsteady boundary-layer transition against α over the experimental range of Re_c, for α^+ = 0.08. For all three Re_c, transition was first observed at the sensor farthest aft, at $0.234s/c$, and moved forward with increasing α. Subsequent transition movement with the α increase was similar for all three Re_c. At some intermediate surface location, transition movement gradually decelerated and then halted a short distance forward of this intermediate location. This intermediate location was farther forward and was reached at a lower α for higher Re_c. Higher Re_c consistently accelerated unsteady boundary-layer transition, causing it to occur at lower α. Finally, in Fig. 11, the plot slopes for different Re_c are comparable for corresponding stages in the transition process. This indicates that unsteady boundary-layer transition movement responds with comparable sensitivity to α increments across the range of Re_c. However, transition progression speed increases significantly with increasing Re_c.

Unsteady boundary-layer reversal and transition data from Figs. 8 and 10 have been superimposed in Fig. 12. Similarly, the same types of data from Figs. 9 and 11 have been reproduced in Fig. 13. This has been done to highlight the spatial and temporal relationships between the unsteady boundary-layer reversal and transition processes.

In both Figs. 12 and 13, unsteady boundary-layer reversal consistently precedes transition by a significant α margin. Further, across the range of Re_c and α^+, patterns of transition movement over the airfoil surface strongly resemble those of reversal. In Fig. 12, at $Re_c = 9.2 \times 10^4$, transition profiles are shifted an approximately equal α increment across the range of α^+. This implies shorter intervening times between reversal and transition at higher α^+. In Fig. 13, at α^+ = 0.08, the α increment is smaller at higher Re_c, corresponding to even shorter time delays between unsteady boundary-layer reversal and transition at higher Re_c. Shorter delays between unsteady boundary-layer reversal and transition are consistent with thinner boundary layers and enhanced vorticity concentrations associated with higher Re_c and α^+.[17]

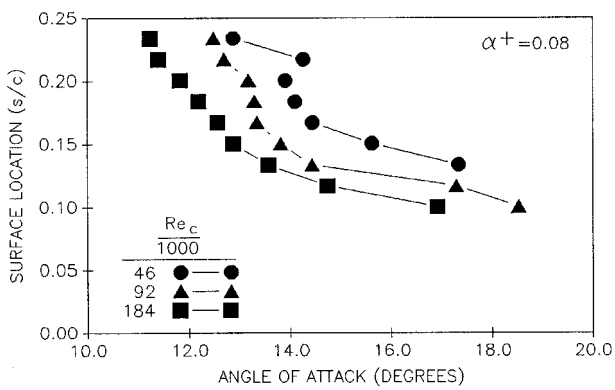

Fig. 11 Summary plot of unsteady boundary-layer transition location vs α for α^+ = 0.08 and experimental range of Re_c.

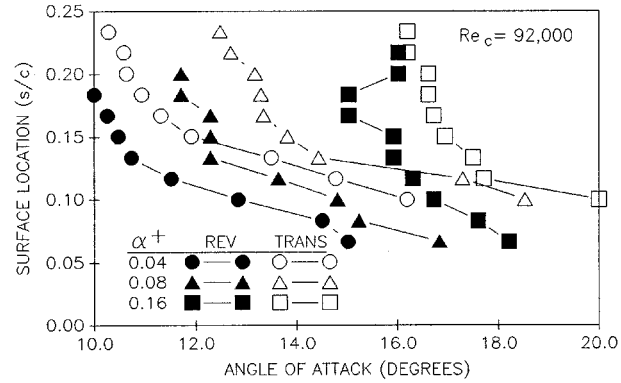

Fig. 12 Summary plot of unsteady boundary-layer reversal and transition location vs α for $Re_c = 9.2 \times 10^4$ and experimental range of α^+.

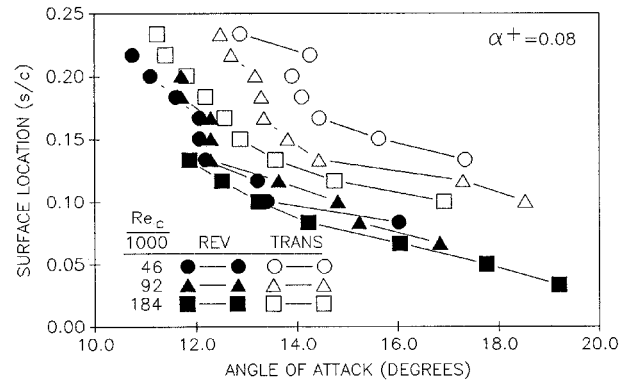

Fig. 13 Summary plot of unsteady boundary-layer reversal and transition location vs α for α^+ = 0.08 and experimental range of Re_c.

Conclusions

A two-dimensional NACA 0015 airfoil was pitched at constant rate through static stall to elevated angles of attack. Unsteady shear stress measurements of high spatial and temporal resolution were acquired in the airfoil leading-edge region. Unsteady boundary-layer transition and boundary-layer reversal were characterized in detail across a range of α^+ and Re_c. These data and data analyses quantified the independent influences of α^+ and Re_c upon unsteady boundary-layer reversal and transition. Unsteady boundary-layer reversal and transition responded in a consistent and orderly fashion to parameter variations.

Unsteady Boundary-Layer Reversal

Increasing α^+ delays unsteady boundary-layer reversal to higher α, tends to confine reversal to the leading-edge region, and accelerates reversal movement over the surface. Higher Re_c delays unsteady boundary-layer reversal to higher α, and simultaneously drives reversal closer to the leading edge and spatially compresses this event along the surface.

Unsteady Boundary-Layer Transition

Increasing α^+ delays unsteady boundary-layer transition to higher α. Higher Re_c causes unsteady boundary-layer transition to occur at lower α. Transition moves forward more rapidly over the airfoil surface in response to both higher α^+ and Re_c.

Sequence of Reversal and Transition

Unsteady boundary-layer reversal precedes unsteady boundary-layer transition at the low and transitional Reynolds numbers employed in the current investigation. Patterns of transition movement over the airfoil surface strongly resemble those of reversal. Higher α^+ and Re_c shortened the delay time between unsteady boundary-layer reversal and transition. The reverse flow in the unsteady boundary constitutes a strong destabilizing influence and is a principal contributor to unsteady boundary-layer transition.

These investigations have characterized unsteady boundary-layer processes that precede and shape the global character of dynamically separated flowfields. This knowledge is a first step toward establishing a basis for controlling and exploiting dynamically separated flows for maneuvering aircraft, rotorcraft, and wind energy machines.

References

[1]Carr, L. W., "Progress in Analysis and Prediction of Dynamic Stall," *Journal of Aircraft*, Vol. 25, No. 1, 1988, pp. 6–17.

[2]Carr, L. W. (ed.), "Physics of Forced Unsteady Boundary Layer Reversal," NASA Ames Research Center, NASA CP 3144, Moffett Field, CA, April 1990.

[3]Carr, L., McAlister, K., and McCroskey, W., "Analysis of the Development of Dynamic Stall Based on Oscillating Airfoil Experiments," NASA TN D-8382, Jan. 1977.

[4]Schreck, S., and Luttges, M., "Occurrence and Characteristics of Flow Reversal During the Genesis of Unsteady Separated Flows," AIAA Paper 89-0142, Jan. 1989.

[5]Visbal, M. R., "On Some Physical Aspects of Airfoil Dynamic Stall," American Society of Mechanical Engineers Symposium on Non-Steady Fluid Dynamics, Toronto, Canada, June 1990.

[6]Ghia, K., Yang, J., Osswald, G., and Ghia, U., "Study of the Role of Unsteady Boundary Layer Reversal in the Formation of Dynamic Stall Vortex," AIAA Paper 92-0196, Jan. 1992.

[7]Knight, D., and Choudhuri, P., "2-D Unsteady Leading Edge Boundary Layer Reversal on a Pitching Airfoil," AIAA Paper 93-2977, July 1993.

[8]Ericsson, L. E., "What About Transition Effects?," AIAA Paper 88-0564, Jan. 1988.

[9]Lorber, P., and Carta, F., "Unsteady Transition Measurements on a Pitching Three-Dimensional Wing," 5th Symposium on Numerical and Physical Aspects of Aerodynamic Flows, California State Univ., Long Beach, CA, Jan. 1992.

[10]Wilder, M., Chandrasekhara, M., and Carr, L.,"Transition Effects on Compressible Dynamic Stall of Transiently Pitching Airfoils," AIAA Paper 93-2978, July 1993.

[11]Carr, L., and Cebeci, T., "Boundary Layers on Oscillating Airfoils," 3rd Symposium on Numerical and Physical Aspects of Aerodynamic Flows, California State Univ., Long Beach, CA, Jan. 1985.

[12]Stack, J., Mangalam, S., and Kalburgi, V., "The Phase Reversal Phenomenon at Flow Separation and Reattachment," AIAA Paper 88-0408, Jan. 1988.

[13]Mangalam, S., Stack, J., and Sewall, W., "Simultaneous Detection of Separation and Transition in Surface Shear Layers," *AGARD Fluid Dynamics Panel Symposium*, CP-438, AGARD, 1988.

[14]Robinson, M., Walker, J., and Wissler, J., "Unsteady Surface Pressure Measurements on a Pitching Rectangular Wing," *Proceedings of Workshop II on Unsteady Separated Flow*, U.S. Air Force Academy, CO, 1988, pp. 225–237.

[15]Schreck, S., Addington, G., and Luttges, M., "Flow Field Structure and Development near the Root of a Straight Wing Pitching at Constant Rate," AIAA Paper 91-1793, June 1991.

[16]Gendrich, C., Koochesfahani, M., and Visbal, M., "Initial Acceleration Effects on the Flow Field Development Around Rapidly Pitching Airfoils," AIAA Paper 93-0438, Jan. 1993.

[17]Robinson, M., and Wissler, J., "Pitch Rate and Reynolds Number Effects on a Pitching Rectangular Wing," AIAA Paper 88-2577, June 1988.

[18]Luttges, M., and Kennedy, D., "Initiation and Use of Three-Dimensional Unsteady Separated Flows," *Proceedings of Workshop II on Unsteady Separated Flow*, U.S. Air Force Academy, CO, 1988, pp. 211–222.